

Cite this: *Chem. Sci.*, 2015, **6**, 3026

Theoretical studies on the photophysical properties of luminescent pincer gold(III) arylacetylide complexes: the role of π -conjugation at the C-deprotonated $[\text{C}^{\text{N}}\text{C}]$ ligand†

Glenna So Ming Tong,^{*a} Kaai Tung Chan,^a Xiaoyong Chang^a and Chi-Ming Che^{*ab}

We have performed theoretical analyses of the photophysical properties of a series of cyclometalated gold(III) arylacetylide complexes, $[(\text{C}^{\text{N}}\text{C})\text{Au}^{\text{III}}\text{C}\equiv\text{CPh-4-OMe}]$, with different extents of π -conjugation at the doubly C-deprotonated $[\text{C}^{\text{N}}\text{C}]$ ligand via replacement of one of the phenyl moieties in the non-conjugated $\text{C}_\text{H}^{\text{N}}\text{C}$ ligand (**1**) by a naphthalenyl (**2**) or a fluorenyl moiety (**3-exo** and **3-endo**; $\text{HC}_\text{H}^{\text{N}}\text{CH} = 2,6\text{-diphenylpyridine}$). Conforming to the conventional wisdom that extended π -conjugation imposes rigidity on the structure of the ${}^3\text{IL}(\pi\pi^*(\text{C}^{\text{N}}\text{C}))$ excited state ($\text{IL} = \text{intraligand}$), the calculated Huang–Rhys factors for the ${}^3\text{IL} \rightarrow S_0$ transition follow the order: **1** > **2** > **3-exo** ~ **3-endo**, which corroborates *qualitatively* the experimental non-radiative decay rate constants, k_{nr} : **1** \gg **2** > **3-exo**, but not **3-endo**. Density Functional Theory (DFT) calculations revealed that there is an additional triplet excited state minimum of ${}^3\text{LLCT}$ character ($\text{LLCT} = \text{ligand-to-ligand charge transfer}$; ${}^3[\pi(\text{C}\equiv\text{CPh-4-OMe}) \rightarrow \pi^*(\text{C}^{\text{N}}\text{C})]$) for complexes **1** and **3-endo**. This ${}^3\text{LLCT}$ excited state, possessing a large out-of-plane torsional motion between the planes of the $\text{C}^{\text{N}}\text{C}$ and arylacetylide ligands, has a double minimum anharmonic potential energy surface along this torsional coordinate which leads to enhanced Franck–Condon overlap between the ${}^3\text{LLCT}$ excited state and the ground state. Together with the larger spin-orbit coupling (SOC) and solvent reorganization energy for the ${}^3\text{LLCT} \rightarrow S_0$ transition compared with those for the ${}^3\text{IL} \rightarrow S_0$ transition, the calculated k_{nr} values for the ${}^3\text{LLCT} \rightarrow S_0$ transition are more than 690- and 1500-fold greater than the corresponding ${}^3\text{IL} \rightarrow S_0$ transition for complexes **1** and **3-endo** respectively. Importantly, when this ${}^3\text{LLCT} \rightarrow S_0$ decay channel is taken into consideration, the non-radiative decay rate constant k_{nr} could be reproduced *quantitatively* and in the order of: **1** \gg **3-endo**, **2** > **3-exo**. This challenges the common view that the facile non-radiative decay rate of transition metal complexes is due to the presence of a low-lying metal-centred ${}^3\text{dd}$ or ${}^3\text{LMCT}$ excited state ($\text{LMCT} = \text{ligand-to-metal charge transfer}$). By analysis of the relative order of MOs of the chromophoric $[\text{C}^{\text{N}}\text{C}]$ cyclometalated and arylacetylide ligands, one may discern why complexes **1** and **3-endo** have a low-lying ${}^3\text{LLCT}$ excited state while **3-exo** does not.

Received 28th November 2014
Accepted 9th March 2015DOI: 10.1039/c4sc03697b
www.rsc.org/chemicalscience

Introduction

Gold(III) complexes are being actively studied as potential anticancer drugs¹ and catalysts.^{2,3} However, the study of the

spectroscopic and luminescent properties of gold(III) complexes is still in its infancy, in particular when compared to their isoelectronic platinum(II) counterparts, which are known to display rich photophysical behaviours. One of the impediments to the progress of photoluminescence of gold(III) complexes is the high electrophilicity of the gold(III) ion and the presence of a low-lying $\text{Au}(5\text{d}\sigma^*)$ orbital. In effect, the deactivating ligand-to-metal charge transfer (LMCT) and/or dd ligand-field excited states become close in energy to the emitting excited state, leading to efficient luminescence quenching in gold(III) complexes.⁴ To circumvent this problem, Yam and co-workers have coupled various strong σ -donating ligands, such as arylacetylide and *N*-heterocyclic carbenes (NHC), to the gold(III) cyclometalated complexes;

^aState Key Laboratory of Synthetic Chemistry, Institute of Molecular Functional Materials, Department of Chemistry, The University of Hong Kong, Pokfulam Road, Hong Kong SAR, China. E-mail: tongsm@hku.hk; cmche@hku.hk

^bHKU Shenzhen Institute of Research and Innovation, Shenzhen 518053, China. E-mail: cmche@hku.hk

† Electronic supplementary information (ESI) available: Experimental details of synthesis, characterization, and photophysical properties of complex **3-endo**, additional computational details, and the Cartesian coordinates of the optimized structures. CCDC 1034529. For ESI and crystallographic data in CIF or other electronic format see DOI: 10.1039/c4sc03697b

these complexes were reported to be weakly emissive in solution ($\phi < 0.01$) at room temperature.⁵

To enhance the emission quantum yield, the structural distortion between the emitting excited state and the ground state must be minimized, thereby decreasing the non-radiative decay rate.⁶ This can be achieved by designing emitting molecules with highly rigid ligand scaffolds, for example, by extended π -conjugation at the cyclometalated ligand⁷ (see Table 1 for a comparison between the emission quantum yields of selected examples of gold(III) cyclometalated complexes with different extents of π -conjugation at the $[C^N^C]$ ligand).^{3a,5,8} A particularly striking example is the series of gold(III) complexes with a fluorenyl moiety incorporated into the doubly deprotonated $[C^N^C]$ ligand.^{3a} In this case, the room temperature emission quantum yields of the gold(III) cyclometalated complexes in solution reach 0.58, and the corresponding non-radiative decay rate constant (k_{nr}) falls to $1.74 \times 10^3 \text{ s}^{-1}$ (Table 1, column 5). In other words, k_{nr} drops more than four orders of magnitude when one of the phenyl moieties in the non-conjugated C^N^C ligand (Table 1, column 2; $HC^N^CCH = 2,6$ -diphenylpyridine) is replaced by a fluorenyl moiety.^{3a} Similar enhancement in emission quantum yield has also been reported for fluorene-functionalized cyclometalated platinum(II) complexes when compared with the non-conjugated C^N^C analogue;⁹ the enhanced luminescence is attributed to the rigid π -conjugated fluorene unit which minimizes structural distortion between the emitting triplet excited state and the ground state.

Interestingly, when the fluorenyl moiety is disposed in such a fashion that the long alkyl chains are “endo” in the gold(III) pincer complex (last column in Table 1), there is a dramatic decrease in emission quantum yield ($\phi \sim 0.02$, $\tau \sim 14.5 \mu\text{s}$) and a nearly 40-fold increase in the non-radiative decay rate constant ($k_{nr} \sim 6.76 \times 10^4 \text{ s}^{-1}$) when compared

with its “exo” analogue (Table 1, column 5; see ESI† for the synthetic procedure and photophysical properties of the “endo” complex). This means that, even with a seemingly suitable cyclometalated ligand (*i.e.*, a strong σ -donor which raises the energy of the dd or LMCT excited state and a cyclometalated ligand with extended π -conjugation that minimizes structural distortion), the phosphorescence efficiency of gold(III) complexes is not necessarily high. Thus, for effective design of functional luminescent molecules, it is important to understand the effect of π -conjugation in the C-deprotonated cyclometalated $[C^N^C]$ ligand on the excited state properties of these luminescent gold(III) complexes.

In this work, we have performed a detailed theoretical analysis of four gold(III) complexes with different $[C^N^C]$ cyclometalated ligand scaffolds (Chart 1), namely, the non-conjugated C^N^C (**1**) and the π -conjugated $C_{np}^N^C$ (**2**) and $C_{fl}^N^C$ (**3-exo** and **3-endo**); complexes **2** and **3-exo** (and **3-endo**) have one of the phenyl moieties of **1** replaced by a naphthalenyl (np) or a fluorenyl (fl) moiety respectively. The ancillary ligand, *p*-methoxyphenyl acetylidyde ($[C\equiv CPh-4-OMe]^-$) is kept the same for all four complexes. A detailed list of definitions and abbreviations is provided in the appendix.

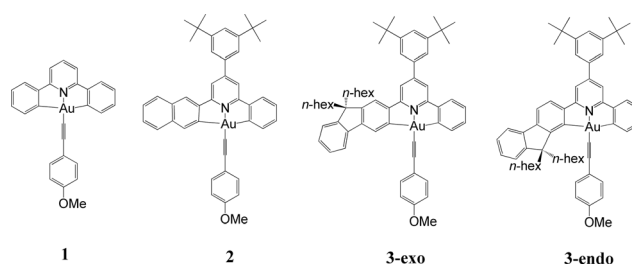


Chart 1

Table 1 Photophysical properties of gold(III) pincer-type complexes in dichloromethane solution at room temperature. For $R = C\equiv CPh-4-OMe$, $n = 0$ and for $R = 1,3$ -dimethylimidazol-2-ylidene, $n = 1$. $C_x^N^C$ = pincer-type cyclometalated ligand; $X = H$, np, or fl

	$[Au^{III}(C^N^C)R]^n$	$[Au^{III}(C_{np}^N^C)R]^n$	$[Au^{III}(C_{fl}^N^C)R]^n$	<i>exo</i> - $[Au^{III}(C_{fl}^N^C)R]^n$	<i>endo</i> - $[Au^{III}(C_{fl}^N^C)R]^n$
$R =$	$\phi = 0.0004$ $\tau = 0.017 \mu\text{s}^{3a,5b}$ $k_{nr} = 5.88 \times 10^7 \text{ s}^{-1}$	$\phi = 0.08$ $\tau = 64 \mu\text{s}^{8a}$ $k_{nr} = 1.44 \times 10^4 \text{ s}^{-1}$	$\phi = 0.09$ $\tau = 25 \mu\text{s}^{8a}$ $k_{nr} = 3.64 \times 10^4 \text{ s}^{-1}$	$\phi = 0.58$ $\tau = 242 \mu\text{s}^{3a}$ $k_{nr} = 1.74 \times 10^3 \text{ s}^{-1}$	$\phi = 0.02$ $\tau = 14.5 \mu\text{s}$ (this work) $k_{nr} = 6.76 \times 10^4 \text{ s}^{-1}$
$R =$	$\text{MeO}-\text{C}_6\text{H}_4-\text{C}\equiv\text{C}-$	$\text{MeO}-\text{C}_6\text{H}_4-\text{C}\equiv\text{C}-$	$\text{MeO}-\text{C}_6\text{H}_4-\text{C}\equiv\text{C}-$	$\text{MeO}-\text{C}_6\text{H}_4-\text{C}\equiv\text{C}-$	$\text{MeO}-\text{C}_6\text{H}_4-\text{C}\equiv\text{C}-$
$R =$	$\text{MeO}-\text{C}_6\text{H}_4-\text{C}\equiv\text{C}-$	$\text{MeO}-\text{C}_6\text{H}_4-\text{C}\equiv\text{C}-$	$\text{MeO}-\text{C}_6\text{H}_4-\text{C}\equiv\text{C}-$	$\text{MeO}-\text{C}_6\text{H}_4-\text{C}\equiv\text{C}-$	$\text{MeO}-\text{C}_6\text{H}_4-\text{C}\equiv\text{C}-$
$R =$	$\text{MeO}-\text{C}_6\text{H}_4-\text{C}\equiv\text{C}-$	$\text{MeO}-\text{C}_6\text{H}_4-\text{C}\equiv\text{C}-$	$\text{MeO}-\text{C}_6\text{H}_4-\text{C}\equiv\text{C}-$	$\text{MeO}-\text{C}_6\text{H}_4-\text{C}\equiv\text{C}-$	$\text{MeO}-\text{C}_6\text{H}_4-\text{C}\equiv\text{C}-$

Theoretical background

Dynamical solvent effect on excited state and ground state energies

Density Functional Theory (DFT) and time-dependent DFT (TDDFT) are the commonly used tools to study the ground state and excited state properties of medium- to large-sized molecules. In the literature, computation of emission energies in solutions is performed using either linear response TDDFT (LR-TDDFT) or the Δ SCF method. For both types of calculations, both the excited state of interest and the ground state are calculated with equilibrium (EQ) solvation. However, in an emission process, the ground state should be treated with solvent polarization in the non-equilibrium (NEQ) regime¹⁰ because the time scale of an emission process is much faster than that of the solvent dynamics. Therefore, for a rigorous consideration of the solvent effect on an emission process, the ground state should be computed with *non-equilibrium* solvation, *i.e.*, only the solvent electronic polarization (the “fast” component) is in equilibrium with the ground state electron density of the solute, while the solvent nuclear polarization (the “slow” component) remains equilibrated with the excited state electron density of the solute. For this reason, we have employed the state-specific (SS) approach to account for the dynamical solvent effect. Within the SS scheme, rather than using the *ground state* electronic density as in LR-TDDFT and Δ SCF, the electronic density of the *emitting excited state* is used to compute the ground state energy.¹⁰ Therefore, the emission energy within the SS scheme ($\Delta E_{\text{em}}^{\text{SS}}$) is given by:

$$\Delta E_{\text{em}}^{\text{SS}} = E_{\text{EQ}}^{\text{ES}}(Q_0^{\text{ES}}) - E_{\text{NEQ}}^{\text{GS}}(Q_0^{\text{ES}}) \quad (1)$$

$E_{\text{EQ}}^{\text{ES}}(Q_0^{\text{ES}})$ is the energy of the excited state (ES) with equilibrium solvation at the optimized excited state geometry (Q_0^{ES}), and $E_{\text{NEQ}}^{\text{GS}}(Q_0^{\text{ES}})$ is the energy of the ground state (GS) with non-equilibrium solvation at (Q_0^{ES}) (Fig. 1).¹¹

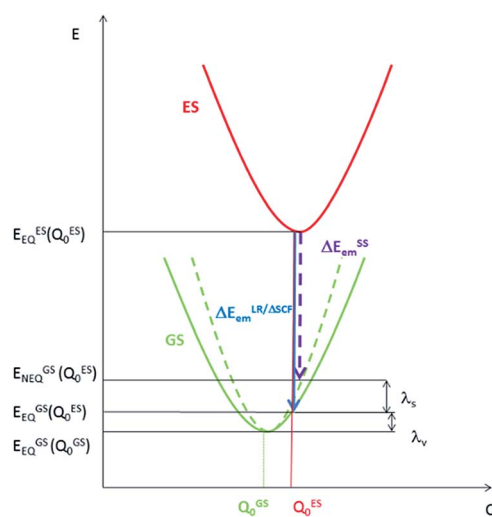


Fig. 1 Potential energy surfaces for an electronic transition with energy evaluated with equilibrium solvation (solid line) and non-equilibrium solvation (dashed line).

The SS approach also allows one to estimate the solvent reorganization energy (λ_s), which is the ground state energy difference calculated with *non-equilibrium* solvation ($E_{\text{NEQ}}^{\text{GS}}(Q_0^{\text{ES}})$) and with *equilibrium* solvation ($E_{\text{EQ}}^{\text{GS}}(Q_0^{\text{ES}})$) at the optimized *excited state geometry* (Q_0^{ES}) (Fig. 1):¹¹

$$\lambda_s = E_{\text{NEQ}}^{\text{GS}}(Q_0^{\text{ES}}) - E_{\text{EQ}}^{\text{GS}}(Q_0^{\text{ES}}) \quad (2)$$

Similarly, the intramolecular reorganization energy computed within the SS approach (λ_v^{SS}) is given by:

$$\lambda_v^{\text{SS}} = E_{\text{EQ}}^{\text{GS}}(Q_0^{\text{ES}}) - E_{\text{EQ}}^{\text{GS}}(Q_0^{\text{GS}}) \quad (3)$$

where $E_{\text{EQ}}^{\text{GS}}(Q_0^{\text{GS}})$ is the energy of the ground state computed with *equilibrium* solvation at the optimized *ground state geometry* Q_0^{GS} (Fig. 1).

Radiative decay rate constant (k_r)

The total radiative decay rate constant from the vibrational ground state of the emitting T_1 α -spin sub-state (k_r^α) to the S_0 state vibrational manifolds is given by the sum of individual radiative decay rate constants (denoted $k_r^\alpha(\tilde{\nu})$), each corresponding to a single vibronic transition, $T_1^\alpha(v' = 0) \rightarrow S_0(v'')$, with photon energy, $\tilde{\nu}$, and vibrational quantum number for the T_1 and S_0 states, v' and v'' , respectively:

$$k_r^\alpha(T_1 \rightarrow S_0) = \sum_{\tilde{\nu}} k_r^\alpha(\tilde{\nu}) \quad (4)$$

The radiative decay rate constant for the single vibronic transition can be calculated from the Einstein coefficient of spontaneous emission:¹²

$$k_r^\alpha(\tilde{\nu}) = \frac{8\pi^2\eta^3\tilde{\nu}^3}{3\varepsilon_0\hbar} |\mathbf{M}_{T^\alpha}(Q)|^2 \quad (5)$$

where η is the solvent refractive index, $\tilde{\nu}$ is the triplet emission energy (in cm^{-1}), and $\mathbf{M}_{T^\alpha}(Q)$ is the transition dipole moment of the $T_1^\alpha \rightarrow S_0$ transition (in ea_0), and the prefactor $8\pi^2/3\varepsilon_0\hbar = 2.0261 \times 10^{-6}$.

By invoking the Condon approximation (*i.e.*, $\mathbf{M}_{T^\alpha}(Q) \approx \mathbf{M}_{T^\alpha}(Q_0^{\text{T1}})$ with Q_0^{T1} being the optimized T_1 excited state geometry) and combining eqn (4) and (5), the total radiative decay rate constant, k_r^α , is given by:¹³

$$k_r^\alpha(T_1 \rightarrow S_0) = \frac{8\pi^2\eta^3}{3\varepsilon_0\hbar} |\mathbf{M}_{T^\alpha}(Q_0^{\text{T1}})|^2 \sum_{\tilde{\nu}} \tilde{\nu}^3 \left| \int \chi_{v''}^* \chi_{v'} dQ \right|^2 \quad (6)$$

$\chi_{v''}$ and $\chi_{v'}$ are the vibrational wavefunctions of the S_0 and the T_1 states respectively.

Unless the emission spectrum is sharply peaked, as in an atomic emission spectrum, one should not take the integral in eqn (6) as unity and replace the summation in eqn (6) by the emission peak maximum, $\tilde{\nu}_{\text{max}}^3$; such an approximation is justified only if the molecule has fixed nuclei. In reality, however, the nuclei are in motion, bringing about a broadening of the emission spectrum. These nuclear motions (*i.e.*, vibrations) can be accounted for by the Franck–Condon factors

$(|\int \chi_{v''}^* \chi_{v'} dQ|^2)$. In general, one may approximate the last term in the summation as:¹³

$$\sum_{\tilde{\nu}} \tilde{\nu}^3 \left| \int \chi_{v''}^* \chi_{v'} dQ \right|^2 = \langle \tilde{\nu}^3 \rangle_{\text{ref}} = \frac{\int I(\tilde{\nu}) d\tilde{\nu}}{\int \tilde{\nu}^{-3} I(\tilde{\nu}) d\tilde{\nu}} \quad (7)$$

with $I(\tilde{\nu})$ being the emission intensity at $\tilde{\nu}$ (corrected to the number of photons emitted per unit wavenumber). The emission intensity can be obtained either from experiment or by computational simulation. The total radiative decay rate constant for the $T_1^\alpha \rightarrow S_0$ transition may then be written as:

$$k_r^\alpha(T_1 \rightarrow S_0) = \frac{8\pi^2 \eta^3 \langle \tilde{\nu}^3 \rangle_{\text{ref}}}{3\epsilon_0 \hbar} |\mathbf{M}_{T^\alpha}(Q_0^{T_1})|^2 \quad (8)$$

The transition dipole moment $\mathbf{M}_{T^\alpha}(Q_0^{T_1})$ could be obtained by first-order perturbation interactions between the T_1 α -spin sub-state and the singlet excited state *via* spin-orbit coupling (SOC):¹²

$$\mathbf{M}_{T^\alpha}(Q_0^{T_1}) = \sum_{j \in x,y,z} \left| \sum_m \frac{\langle T_1^\alpha | H_{\text{SOC}} | S_m \rangle}{E(S_m) - E(T_1)} \mathbf{M}_{S_{m,j}}(Q_0^{T_1}) \right|^2 \quad (9)$$

where $\mathbf{M}_{S_{m,j}}$ is the j -axis projection of the $S_m \rightarrow S_0$ transition dipole moment, $E(T_1)$ and $E(S_m)$ are the energies of the T_1 and the m^{th} singlet (S_m) excited states, respectively, and $\langle T_1^\alpha | H_{\text{SOC}} | S_m \rangle$ are the SOC matrix elements between the T_1 α -spin sub-state and the S_m excited state.

As the energy splitting between the three T_1 α -spin sub-states is less than 5 cm^{-1} , all sub-states should be equally populated at room temperature. Therefore, the average radiative decay rate constant k_r is given by:

$$k_r(T_1 \rightarrow S_0) = \frac{1}{3} \sum_{\alpha} k_r^\alpha \quad (10)$$

Non-radiative decay rate constant (k_{nr})

In the limit of the Franck–Condon approximation in the non-adiabatic regime, the non-radiative decay rate constant (k_{nr}) of the $T_1 \rightarrow S_0$ transition can be estimated by application of the Fermi's Golden Rule expression, assuming that both electronic states are harmonic:¹⁴

$$k_{\text{nr}}(T_1 \rightarrow S_0) = \frac{2\pi}{\hbar} \frac{\langle T_1 | H_{\text{SOC}} | S_0 \rangle^2}{(4\pi\lambda_s k_B T)^{\frac{1}{2}}} \times \sum_{n_M}^{\infty} \frac{S_M}{n_M!} \exp(-S_M) \times \exp\left(-\frac{(\Delta E - n_M \hbar\omega_M - \lambda_s)^2}{4\lambda_s k_B T}\right) \quad (11)$$

This expression can be applied when $\hbar\omega_M \gg k_B T$ and the solvent orientational and librational motions are treated classically. ω_M are the high-frequency (hf) intraligand vibrational modes ($\hbar\omega_M > 1000 \text{ cm}^{-1}$), typically corresponding to the aromatic CC/CN stretching modes ($\hbar\omega_M \sim 1200\text{--}1500 \text{ cm}^{-1}$) and C≡C stretching modes ($\hbar\omega_{\text{C}\equiv\text{C}} \sim 2200\text{--}2300 \text{ cm}^{-1}$) if the

acetylide ligand is involved in the complex; λ_s is the solvent reorganization energy and may be obtained from eqn (2); ΔE is given by

$$\Delta E = \Delta E_{00} - \lambda_{\text{lf}} \quad (12a)$$

with ΔE_{00} being the zero-point energy difference between the T_1 and S_0 states and λ_{lf} being the reorganization energy contributed by the low-frequency (lf) modes of the complex (*i.e.*, $\hbar\omega_{\text{lf}} < 1000 \text{ cm}^{-1}$). Assuming that all the normal modes are harmonic oscillators,

$$\lambda_{\text{lf}} = \sum_{j \in \text{lf}} S_j \hbar\omega_j \quad (12b)$$

$$S_j = \frac{1}{2} \left(\frac{m_j \omega_j}{\hbar} \right) \Delta Q_j^2 \quad (12c)$$

S_j , m_j , and ΔQ_j are the Huang–Rhys factor, the reduced mass, and the equilibrium displacement of the j^{th} normal mode ω_j , respectively; S_M and n_M are the Huang–Rhys factor and the number of quanta of the effective high frequency mode $\hbar\omega_M$ (corrected to the nearest integer), respectively:

$$S_M = \sum_{j \in \text{hf}} S_j \quad (12d)$$

$$n_M = \frac{\Delta E - \lambda_s}{\hbar\omega_M} \quad (12e)$$

Under the harmonic oscillator approximation, the intramolecular reorganization energy, λ_v^{FC} , could be estimated as:

$$\lambda_v^{\text{FC}} = \sum_j S_j \hbar\omega_j \quad (13)$$

where the summation runs over all the normal modes, ω_j .

Computational details

In this work, the hybrid density functional, PBE0,¹⁵ was employed for all calculations using the program package G09.¹⁶ The 6-31G* basis set¹⁷ was used for all atoms except Au, which was described by the Stuttgart relativistic pseudopotential and its accompanying basis set (ECP60MWB).¹⁸ The solvent effect was also included by means of the polarizable continuum model (PCM) with the solvent as dichloromethane (CH_2Cl_2 ; $\eta = 1.424$).¹⁹ Geometry optimizations of the singlet ground state (S_0) and the lowest triplet excited state (T_1) were respectively carried out using restricted and unrestricted density functional theory (*i.e.*, RDFT and UDFT) formalisms without symmetry constraints. Frequency calculations were performed on the optimized structures to ensure that they were minimum energy structures by the absence of imaginary frequency (*i.e.*, $\text{NIImag} = 0$). Stability calculations were also performed for all the optimized structures to ensure that all the wavefunctions obtained were stable.

Vertical transition energies were computed using the linear response approximation for absorption, but the state specific approach for emission.²⁰ For the radiative decay rate constant calculation (using eqn (8) and (9)), the singlet excited state energy, $E(S_m)$, the associated transition dipole moment of the



$S_m \rightarrow S_0$ transition $M_{S_m j}$ ($j = x, y, z$), and the coefficients necessary to compute the SOC matrix elements (*i.e.*, the d-orbital coefficients (c_d) of Au in the MO relevant to the coupling excited states and the corresponding CI coefficients), were all obtained from a state-specific approach using “External-Iteration” implemented in G09.^{10b,20}

The Huang–Rhys factor S_j (using eqn (12c)) for the normal mode ω_j may be obtained by performing a Franck–Condon calculation implemented in G09 *via* “freq = fc” and “prtm = 2”. The simulated emission spectrum allows one to calculate the Franck–Condon factor-weighted emission energy $\langle \tilde{\nu} \rangle_{\text{ef}}$ (using eqn (7)). The high-frequency normal modes ($1000 < \hbar\omega_m \leq 1800 \text{ cm}^{-1}$) can be characterized by a mean frequency ω_M and an effective electron-phonon coupling strength (or Huang–Rhys factor) S_M :²¹

$$S_M = \sum_{j \in m} S_j \quad (14a)$$

$$\lambda_M = \sum_{j \in m} S_j \hbar \omega_j \quad (14b)$$

$$\hbar \omega_M = \frac{\lambda_M}{S_M} \quad (14c)$$

Further computational details can be found in the ESI.[†]

Results and discussion

Ground state structures and absorption energies

In general, the optimized ground state structures of **1**, **3-exo**, and **3-endo** are in good agreement with the X-ray crystallography data ($<0.05 \text{ \AA}$ and 8.5°) except for the dihedral angle between the planes of the $[\text{C}^{\text{N}}\text{C}]$ ligand and the phenyl ring of the acetylidyne ligand (δ); calculations revealed a nearly coplanar geometry ($\delta \sim 5.7^\circ$ and -0.27° for **1** and **3-exo** respectively) whereas experimentally determined δ values are 66.1° and 54° respectively.^{3a,5b} Similarly, though DFT calculations predict a non-coplanar geometry for the ground state of **3-endo** ($\delta \sim 130^\circ$), the corresponding X-ray data is only $\sim 59^\circ$ (see ESI[†] for the X-ray data and DFT results for **3-endo**). In addition, the Au–C(acetylidyne) distance for **1** was calculated to be 1.950 \AA while the corresponding distance from the crystallography data is

2.009 \AA .^{5b} It should be noted that the Au–C(acetylidyne) distances reported for similar $[(\text{C}_\text{H}^{\text{N}}\text{C})\text{Au}^{\text{III}}\text{C}\equiv\text{CPh-4-Y}]$ (Y is a substituent) complexes are in the range of 1.945 – 1.980 \AA ; our calculated value falls within this range. It is thus possible that the discrepancies between experimental and calculated geometries are due to the crystal packing effect.

Table 2 presents the absorption energies of low-lying singlet excited states at the respective optimized S_0 geometries of the four complexes studied herein. A full list of the TDDFT results can be found in the ESI.[†] In general, the calculated absorption energies are in good agreement with the corresponding experimental absorption peak maxima. Previous TD-B3LYP/CPCM calculations also suggest that the lowest absorption peak of **1** is $^1\text{LLCT}$ in nature (LLCT = ligand-to-ligand charge transfer), with a calculated vertical excitation energy at $\lambda = 408 \text{ nm}$ ($f = 0.23$).^{5b}

As depicted in Table 2, the most conspicuous difference among the four complexes is that, except for **3-exo**, the first singlet excited state (S_1) is a $^1\text{LLCT}$ excited state, derived mainly from the $\text{HOMO} \rightarrow \text{LUMO}$ transition, $^1[\pi(\text{C}\equiv\text{CPh-4-OMe}) \rightarrow \pi^*(\text{C}^{\text{N}}\text{C})]$ (Fig. 2 and ESI[†] for the MO surfaces). On the other hand, for **3-exo**, the S_1 state is predominantly intraligand (IL) in character ($>80\%$); this ^1IL excited state is derived from the $\text{H-1} \rightarrow \text{LUMO}$ transition and is a $^1\pi\pi^*(\text{C}^{\text{N}}\text{C})$ excited state. The difference in the nature of the S_1 excited state among the four complexes can be rationalized as follows: upon increasing the π -conjugation along the series **1**, **2**, **3-endo**, and **3-exo**, H-1 is destabilized and the MO splitting ($\Delta\epsilon$) between HOMO and H-1 decreases from 0.62 eV (**1**) to 0.26 eV (**3-endo**) and 0.20 eV (**3-exo**), (Fig. 2). This decrease in MO splitting results in a decrease in the contribution of the $\text{HOMO} \rightarrow \text{LUMO}$ transition to the S_1 state, but a concomitant increase in percentage of the $\text{H-1} \rightarrow \text{LUMO}$ transition (Table S9[†]). As a result, the predominant contribution to the S_1 state is mainly $^1\text{LLCT}$ in character for **1**, **2**, and **3-endo**, while for **3-exo**, the S_1 state is mainly ^1IL in nature. This decrease in MO splitting not only affects the nature of the lowest singlet excited state, but also significantly impacts the emitting excited state, as described in a later section.

T_1 excited state: radiative and non-radiative decay rates

The experimental photophysical data regarding the emissions of the four gold(III) complexes are listed in Table 3.

Table 2 Singlet excited state energies (λ in nm) and the associated oscillator strengths (f), together with the nature of singlet excited states of the four complexes depicted in Chart 1 at their respective optimized S_0 geometries. $\mu^{\text{GS}}(D)$ is the ground state dipole moment obtained from DFT calculations. The experimental values (λ_{exp} in nm) are listed in the last column

Complexes	S_m	λ	F	Nature ^a	μ^{GS}	λ_{exp}
1	S_1	392	0.251	$^1\text{LLCT}$	6.13	400, 380, 362
	S_2	367	0.0519	$^1\pi\pi^*(\text{C}_\text{H}^{\text{N}}\text{C})$		
2	S_1	401	0.2737	$^1\text{LLCT}$	8.36	396, 380
	S_2	370	0.2623	$^1\pi\pi^*(\text{C}_\text{np}^{\text{N}}\text{C})$		
3-exo	S_1	409	0.1645	$^1\pi\pi^*(\text{C}_\text{f}^{\text{N}}\text{C})/^1\text{LLCT}$	8.09	428, 409
	S_2	401	0.3078	$^1\text{LLCT}/^1\pi\pi^*(\text{C}_\text{f}^{\text{N}}\text{C})$		
3-endo	S_1	426	0.0671	$^1\text{LLCT}$	8.09	430, 409
	S_2	407	0.2505	$^1\pi\pi^*(\text{C}_\text{f}^{\text{N}}\text{C})$		

^a All the singlet excited states have some metal character, but generally less than 10%.



	1	2	3-exo	3-endo
HOMO				
	-5.85 eV	-5.81 eV	-5.82 eV	-5.72 eV
H-1				
	-6.47 eV	-6.23 eV	-6.02 eV	-5.98 eV
$\Delta\epsilon / \text{eV}$	0.62	0.42	0.20	0.26

Fig. 2 Frontier MOs of the four complexes at their respective optimized S_0 geometries together with the HOMO/H – 1 MO splitting, $\Delta\epsilon$.

Table 3 Experimental emission maxima (λ_{max} nm $^{-1}$), quantum yields (ϕ) and lifetimes (τ μs^{-1}) of the four complexes measured in dichloromethane solutions at 298 K. Radiative (k_r) and non-radiative (k_{nr}) decay rates are obtained from $k_r = \phi/\tau$ and $k_{\text{nr}} = 1/\tau - k_r$ and are tabulated in units of ($\times 10^3$ s $^{-1}$)

	λ_{max}	ϕ	τ	k_r	k_{nr}
1 (ref. 3a and 5b)	474	0.0004	0.017	23.5	58 800
2 (ref. 8a)	562	0.09	25	3.60	36.4
3-exo (ref. 3a)	538	0.58	242	2.40	1.74
3-endo ^a	536	0.02	14.5	1.38	67.6

^a This work, ESL.†

As depicted in Table 3, **1** has the fastest radiative and non-radiative decay rate constants, with the latter being more than 800-fold faster than that of the other three complexes. Complex **3-exo** displays the slowest k_{nr} among the four complexes studied herein, while the associated k_r is comparable to the other two complexes with π -conjugation at the [C^NC] cyclometalated ligand (*i.e.*, **2** and **3-endo**).

To understand the emission properties of the four complexes depicted in Chart 1, we have employed unrestricted DFT (UDFT) to optimize their lowest triplet excited states. For **2** and **3-exo**, only one triplet excited state, $^3\pi^*(\text{C}^N\text{C})$ IL excited state, was found. On the other hand, two triplet excited state minima, one ^3IL in character and the other $^3\text{LLCT}$ ($^3[\pi(\text{C}\equiv\text{CPh-4-OMe}) \rightarrow \pi^*(\text{C}^N\text{C})]$), were found for both **1** and **3-endo**. The electron difference density maps (eddms) for the calculated triplet excited states, together with the relative energy splitting between the ^3IL and $^3\text{LLCT}$ excited states for complexes **1** and **3-endo**, are presented in Fig. 3.

Table 4 lists the computed 0–0 transition energies (ΔE_{00}), vertical emission energies ($\Delta E_{\text{em}}^{\text{SS}}$, Fig. 1), Franck–Condon factor-

weighted emission energies ($\langle \tilde{\nu} \rangle_{\text{fcf}}$), and radiative decay rate constants of the optimized T_1 excited states of the four gold(III) complexes studied herein.

(i) Emission energies. With the exception of **2**, there is generally a close correlation between the experimental solution emission maxima (λ_{max}) at room temperature and the calculated ΔE_{00} of the ^3IL excited states of the gold(III) complexes in Chart 1. This suggests that for complexes **1**, **3-exo**, and **3-endo**, the emission maximum may correspond to the 0–0 transition of $^3\text{IL} \rightarrow S_0$. The experimental emission maximum of **2** is at a lower energy than that of **3-exo** (Table 3). For related platinum(II) [C^NC] cyclometalated complexes, the one with a naphthalene moiety at the [C^NC] ligand displays a *higher energy* emission peak than the one with a fluorene unit (*e.g.*, complexes **7** and **8** in ref. 9) and the emitting triplet excited state is assigned as having a mixed $^3\text{IL}/^3\text{MLCT}$ character (MLCT = metal-to-ligand charge transfer).⁹ Our present theoretical analysis is in accordance with these findings on the platinum(II) [C^NC] cyclometalated complexes: ΔE_{00} of the gold(III) complexes is in the order **1** > **2** > **3-endo** ~ **3-exo**. This trend is a manifestation of the increase in π -conjugation at the [C^NC] cyclometalated ligand when one goes from **1** to **2** to **3-endo** and **3-exo**. Increasing π -conjugation destabilizes the $\pi(\text{C}^N\text{C})$ orbital, (see also Fig. 2), thereby decreasing the MO splitting between $\pi(\text{C}^N\text{C})$ and $\pi^*(\text{C}^N\text{C})$ orbitals and leading to a red shift in emission energy of the ^3IL excited state from **1** to **2** to **3-endo** and **3-exo**. The fact that the experimental emission maximum of **2** is lower in energy than those of **3-exo** and **3-endo** may reflect that the emission peak maximum of **2** may not correspond to the 0–0 transition; it may suggest that the structural distortion between the T_1 and S_0 states of **2** is larger than that of **3-exo** and **3-endo** (*vide infra*).



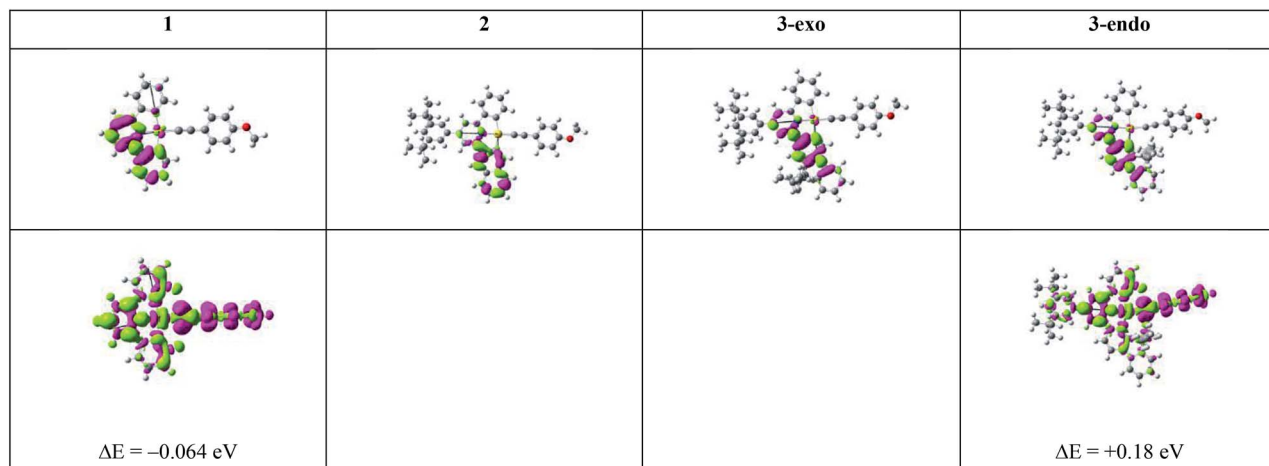


Fig. 3 Electron difference density maps (eddm) as obtained from SS-TDDFT calculations at their respective optimized T_1 excited state geometries for the four complexes in Chart 1 (isovalue = 0.001 a.u.). The upper row depicts the ^3IL excited states while the bottom row presents the $^3\text{LLCT}$ excited states. The ^3IL excited state is set as the reference point, *i.e.*, ΔE (in eV) is the energy of the $^3\text{LLCT}$ excited state relative to that of the ^3IL excited state of a complex obtained from UDFT calculations. Colour scheme: moss green represents increased electron density; magenta represents decreased electron density.

Table 4 Computed 0–0 transition energy (ΔE_{00} in nm), vertical emission energy ($\Delta E_{\text{em}}^{\text{SS}}$ in nm), Franck–Condon-factor weighted emission energy ($\langle \tilde{\nu} \rangle_{\text{fcf}}$ in nm), and radiative decay rate constants ($k_r \times 10^3$ s $^{-1}$) for the four gold(III) complexes^a

		$\Delta E_{\text{em}}^{\text{SS}}$			
		ΔE_{00}	SCF	SS-TDDFT	$\langle \tilde{\nu} \rangle_{\text{fcf}}$
1	^3IL	484	534	612	555 6.12 (8.28)
	$^3\text{LLCT}$	492	586	1832	— ^c 0.018
2	^3IL	541	593	704	618 0.148 (0.219)
	^3IL	554	610	698	621 0.544 (0.772)
3-exo	^3IL	550	604	691	612 0.353 (0.507)
	$^3\text{LLCT}$	510	601	1570	— ^c 0.047

^a $\Delta E_{\text{em}}^{\text{SS}}$ is obtained from two different methods: (1) in the SCF method, it is the energy difference between the T_1 excited state calculated with equilibrium solvation at the UDFT level and the S_0 ground state with non-equilibrium solvation with the T_1 excited state electron density using DFT; (2) in the SS-TDDFT method, it is the pole of the T_1 excited state from a SS-TDDFT calculation with PCM correction; $\langle \tilde{\nu} \rangle_{\text{fcf}}$ is obtained from eqn (7) using the emission spectrum generated from a Franck–Condon calculation implemented in G09 (for details, see above and ESI[†]); k_r is the radiative decay rate constant obtained by considering only the lowest singlet excited state(s) that can have effective SOC with the T_1 excited state (see ESI[†] for further computational details). ^b The value outside the parentheses corresponds to the radiative decay rate constant obtained using SS-TDDFT $\Delta E_{\text{em}}^{\text{SS}}$ while that inside the parentheses corresponds to that obtained using $\langle \tilde{\nu} \rangle_{\text{fcf}}$. ^c FC simulated spectrum is unreliable; and therefore $\langle \tilde{\nu} \rangle_{\text{fcf}}$ cannot be determined in such a case.

(ii) Radiative decay rate constants. Table 4 presents the radiative decay rate constants calculated for each of the T_1 excited states of the four complexes. Although the k_r values of the ^3IL excited states are slightly underestimated by a factor of ~ 2.7 – 3.1 , they are consistent with the experimental k_r values except in the case of 2 (compare Tables 3 with 4). The calculations indicate that 2 should have the slowest radiative decay rate constant, which is not supported by the photophysical data

recorded at room temperature (Table 3). However, it was reported that the emission lifetime of 2 increases from 25 μs at room temperature to 2285 μs in a glassy medium at 77 K.^{8a} Assuming that this lifetime corresponds to the radiative lifetime, k_r would be estimated to have a maximum value of ~ 438 s $^{-1}$. This is close to our theoretical results, *i.e.*, the ^3IL excited state of 2 should have the slowest radiative decay rate constant among the four gold(III) complexes (as a reference, the k_r estimated in the same way as that of 2 at 77 K would be 7.30×10^3 , 3.55×10^3 , and 2.46×10^3 s $^{-1}$ for 1, 3-exo, and 3-endo respectively).^{3a,5b} It is conceivable that the emission of 2 at 298 K and 77 K originated from different excited states. However, no other triplet excited state minimum was found for complex 2 using the present DFT/TDDFT method.

(iii) Non-radiative decay rate constants. Table 5 lists the calculated results related to the non-radiative decay rate constants. First, let us consider the ^3IL excited states of the four gold(III) complexes. As depicted in Table 5, the Huang–Rhys factors (S_M) are in the order: **1** > **2** > **3-exo** \sim **3-endo**. This trend is in line with the S_0 to T_1 structural distortion of the following organic molecules in the order: benzene > naphthalene > carbazole (carbazole is isoelectronic to fluorene).²² These two trends are similar because the ^3IL excited states of these four gold(III) complexes are mainly localized on the phenyl, naphthalenyl, and fluorenyl moieties, respectively (Fig. 3). As the Huang–Rhys factor serves to quantify the structural distortion between the emitting triplet excited state and the ground state, the smallest values of S_M for **3-exo** and **3-endo** reveal that the fluorene unit at the $[\text{C}^{\text{N}}\text{C}]$ cyclometalated ligand imparts the greatest rigidity to the complex. In other words, the rigidity of the organic moiety at the pincer-type cyclometalated ligand could qualitatively account for the experimental results that **1** has the fastest non-radiative decay rate constant and **3-exo** the slowest.

Besides, the magnitude of the SOC matrix element between the ^3IL excited state and S_0 ground state follows the order: **1** > **3-**

Table 5 Effective Huang–Rhys factors (S_M) for the high-frequency mode, intramolecular (λ_v) and solvent (λ_s) reorganization energies (in cm^{-1}), dipole moments of the T_1 excited state (μ^{T_1}/D , $\langle T_1 | H_{\text{SOC}} | S_0 \rangle^2$ (in cm^{-2}), Franck–Condon Factors (FCF), and non-radiative decay rate constants ($k_{\text{nr}} \times 10^3 \text{ s}^{-1}$) for the four complexes studied herein

		λ_v^b		λ_s	μ^{T_1}	$\langle T_1 H_{\text{SOC}} S_0 \rangle^2$	FCF ^e	k_{nr}
		S_M^a	SS					
1	³ IL	1.75	2889	2920	21.2	6.23	943	2.66
	³ LLCT	0.11 ^c	2090	n.a.	1980	16.3	1757	989 ^d
2	³ IL	1.47	2622	2618	62.72	8.36	148	151
3-exo	³ IL	1.29	2392	2408	75.74	7.21	323	9.74
3-endo	³ IL	1.27	2388	2439	83.24	6.29	173	7.24
	³ LLCT	0.22 ^c	2051	n.a.	1812	18.5	1664	1130 ^d
								1880

^a S_M corresponds to the effective Huang–Rhys factor of the high-frequency (hf) modes in the range $1000 \leq \omega_m \leq 1800 \text{ cm}^{-1}$ when the T_1 excited state is ³IL. ^b The intramolecular reorganization energy λ_v was obtained in two different ways: state specific (SS; eqn (3)) and Franck–Condon (FC; eqn (13)). ^c $S_M = S_C$, i.e., the Huang–Rhys factor of the C≡C stretching mode, $\omega_{\text{C}\equiv\text{C}}$ (see ESI† for details). ^d Estimated under the assumption that the Huang–Rhys factors of the ³LLCT \rightarrow S_0 transition are the same as those of the ³IL \rightarrow S_0 of the same complex, together with the Huang–Rhys factor of the C≡C stretching normal mode. ^e The term $2\pi/\hbar$ is absorbed into the FCF.

exo > **3-endo** > **2**. At their respective optimized ³IL excited states, the metal contributions (expressed as c_d^2) to the H – 1 (HOMO for **3-exo** and **3-endo**), at their optimized T_1 geometries, are 4.18 (**1**), 0.36 (**2**), 1.94 (**3-exo**), and 1.07 (**3-endo**), respectively. As SOC is mainly brought about by the gold(III) ion, the larger the coefficient of Au(d) in the H – 1/HOMO, the larger should be the SOC matrix element, $\langle ^3\text{IL} | H_{\text{SOC}} | S_0 \rangle^2$. The Au(d) character in the H – 1/HOMO of the gold(III) complexes studied herein is related to the nature of the HOMO of the C-deprotonated moiety in the [C^N≡C] ligand. For complex **2**, the H – 1 is mainly localized on the *long* molecular axis of the naphthalene fragment (Fig. 2), thus rendering the [C_{np}^N≡C] ligand to have little interaction with the gold(III) ion and therefore, the smallest c_d in the H – 1 orbital of **2**. On the other hand, the corresponding orbital of complex **3-exo** is along the *short* molecular axis of the fluorene fragment, thus the [C_{fl}^N≡C] ligand could have a stronger interaction with the gold(III) ion, and hence, a larger c_d in the HOMOs of complexes **3-exo** and **3-endo**.

Although both the effective Huang–Rhys factor S_M and the SOC between the T_1 and S_0 states are largest for **1**, the calculated non-radiative decay rate constant k_{nr} for the ³IL \rightarrow S_0 transition is *smaller* than that of **3-exo**, a result contrary to the order of experimental k_{nr} values; $k_{\text{nr}}(\text{calc}): 2 > 3\text{-exo} > 1; k_{\text{nr}}(\text{expt}): 1 \gg 2 > 3\text{-exo}$. This is because **1** has a much larger energy gap between the ³IL and S_0 states than the other three gold(III) complexes (Table 4), making the energy gap effect play a dominant role in determining the k_{nr} (³IL \rightarrow S_0) of **1**. Similarly, the calculated non-radiative decay rate constant for **3-endo** is $\sim 1.25 \times 10^3 \text{ s}^{-1}$, which is also *smaller* than that of **3-exo**, and is inconsistent with the experimental data (compare Tables 3 and 5). For these two complexes, **1** and **3-endo**, an additional triplet excited state minimum was found (Fig. 3). This triplet excited state, as observed from the eddms in Fig. 3, is best characterized to be a ³LLCT, ${}^3[\pi(\text{C}\equiv\text{CPh-4-OMe}) \rightarrow \pi^*(\text{C}\equiv\text{N}\equiv\text{C})]$, excited state. This ³LLCT excited state displays a large amplitude motion along the dihedral angle between the [C^N≡C] plane and the arylacetylidene plane (δ): from $\sim -4.132^\circ$ (S_0) to -88.739° (³LLCT) for **1** and from 130.381° (S_0) to 92.352° (³LLCT) for **3-endo** (see Fig. 4 for the optimized structures of the S_0 and ³LLCT excited states for complexes **1** and **3-endo**).

Because of this large amplitude motion, we refrained from performing a Franck–Condon calculation on the ³LLCT \rightarrow S_0 transition, as we have performed for that of the ³IL \rightarrow S_0 . This is because, for the Franck–Condon calculation implemented in G09, the normal modes are represented in Cartesian coordinates. Cartesian coordinates are inadequate to describe large amplitude motions, such as torsions, as this could lead to artificial bond breaking and bond forming at its extreme.²³ For instance, due to the rotation of the phenyl group at the arylacetylidene ligand relative to the [C^N≡C] plane, the C–H bonds on the phenyl ring of the arylacetylidene ligand would be artificially broken if Cartesian coordinates were used to describe the normal modes. This could result in erroneously large Huang–Rhys factors for the C–H stretching modes. However, in reality, there is no C–H bond breaking when one goes from the ³LLCT to the S_0 state. Moreover, such fictitious bond breaking and bond forming will lead to a diffuse Duschinsky matrix, which could lead to an incorrect interpretation of the fast non-radiative decay rate constant due to a large Duschinsky effect.

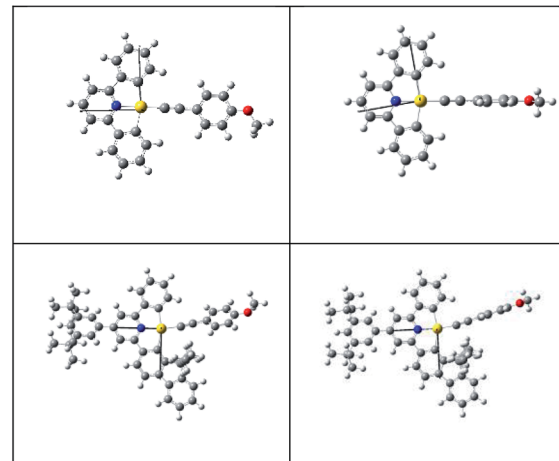


Fig. 4 Optimized structures of the S_0 (left) and ³LLCT excited states for **1** (top) and **3-endo** (bottom).



Nevertheless, the $\text{C}\equiv\text{C}$ stretching normal mode is decoupled from the other normal modes, as reflected by the Duschinsky matrix elements of the ${}^3\text{LLCT} \rightarrow \text{S}_0$ transition; $\omega_{\text{C}\equiv\text{C}}$ is the only normal mode that has the diagonal matrix element equal to 1. Therefore, we estimated the non-radiative decay rate constants of the ${}^3\text{LLCT}$ excited state by replacing all the Huang–Rhys factors (S_j) of the ${}^3\text{LLCT} \rightarrow \text{S}_0$ transition with those of the ${}^3\text{IL} \rightarrow \text{S}_0$ transition, but keeping the Huang–Rhys factor of the $\text{C}\equiv\text{C}$ stretching normal mode from a Franck–Condon calculation of the ${}^3\text{LLCT} \rightarrow \text{S}_0$ transition. Such an assumption is based on the fact that both the ${}^3\text{LLCT}$ and ${}^3\text{IL}$ excited states of the gold(III) complexes involve changes in electron density at the $[\text{C}^{\text{N}}\text{C}]$ ligand.

From Table 5, several points concerning the ${}^3\text{LLCT}$ excited states of **1** and **3-endo** are noted: (a) The solvent reorganization energy (λ_s) of ${}^3\text{LLCT}$ is much larger than that of ${}^3\text{IL}$. This is attributed to the dipole moment of the ${}^3\text{LLCT}$ being much larger than that of ${}^3\text{IL}$ and the ground states (see Table 5 for the excited state dipole moments ($\mu^{\text{T}1}$) and Table 2 for the ground state dipole moments (μ^{GS})). In the framework of the SS approach, solvent reorganization energy is proportional to the square of the difference in dipole moments between the T_1 excited state and the S_0 ground state, *i.e.*, $\lambda_s \propto (\mu^{\text{T}1} - \mu^{\text{GS}})^2$.²⁰ Therefore, this large solvent reorganization effectively leads to a decrease in the energy gap between the ${}^3\text{LLCT}$ and the S_0 potential energy surfaces (PESs) at the equilibrium geometry of the ${}^3\text{LLCT}$ excited state. Thus, fewer quanta of the high-frequency vibrational mode (n_M) are needed (see eqn (12e)) and the activation energy (the temperature-dependent term in the last exponential of eqn (11)) is smaller as this energy term is inversely proportional to the solvent reorganization energy; (b) the square of the H_{SOC} matrix element between the ${}^3\text{LLCT}$ excited state and the S_0 ground state is larger than that between the ${}^3\text{IL}$ excited state and the ground state (Table 5).

The non-radiative decay rate constants thus estimated for the ${}^3\text{LLCT}$ excited states of **1** and **3-endo** are 1.738×10^6 and $1.880 \times 10^6 \text{ s}^{-1}$, respectively, more than 690-fold and over 1500-fold larger than those of their respective ${}^3\text{IL}$ excited states. These non-radiative decay rate constants may still be underestimated since the structural change associated with the torsional motion between the $[\text{C}^{\text{N}}\text{C}]$ and arylacetylide ligands has not been included in the Franck–Condon factor (FCF) calculation of the ${}^3\text{LLCT} \rightarrow \text{S}_0$ transition. (We have used the Huang–Rhys factor of the ${}^3\text{IL} \rightarrow \text{S}_0$ transition where there is no such large amplitude torsion.) We have undertaken a rigid scan along the torsional coordinate (δ) for **1**. Fig. 5a displays the PESs along the torsional coordinate δ for the ground state, ${}^3\text{IL}$ excited state, and ${}^3\text{LLCT}$ excited state of complex **1**. The potential energy minimum is roughly harmonic for both the ground state and the ${}^3\text{IL}$ excited state but anharmonic for ${}^3\text{LLCT}$ excited state. As the ${}^3\text{LLCT}$ excited state has a double minimum potential while the ground state is approximately harmonic, the Franck–Condon factor (FCF) between ${}^3\text{LLCT}$ and S_0 is expected to be larger than that between the ${}^3\text{IL}$ and S_0 states, where both PESs are harmonic along the torsion coordinate δ . This may be rationalized as illustrated in Fig. 5b. The “barrier width” (indicated by the double arrow in Fig. 5b), being qualitatively related

to the FCF in an inverse manner, is smaller for a potential energy surface with a double minimum potential (as in ${}^3\text{LLCT}$ excited state) than that with a harmonic PES (as in ${}^3\text{IL}$ excited state; Fig. 5b).²⁴ Thus, the non-radiative decay rate of the ${}^3\text{LLCT} \rightarrow \text{S}_0$ transition should be further enhanced due to the increase in the FCF brought about by the torsional motion. In addition, there would be a strong thermal quenching of phosphorescence because thermal excitation of the torsional normal mode in the ${}^3\text{LLCT}$ excited state would decrease the “barrier width”, leading to a significant increase in the FCFs, and, hence, a further enhancement of the non-radiative decay rate.

If one supposes that the torsional motion increases the FCF of the ${}^3\text{LLCT} \rightarrow \text{S}_0$ transition by a factor of ~ 10 , the values of k_{nr} for **1** and **3-endo** for this transition would be $\sim 1.7 \times 10^7$ and $\sim 1.9 \times 10^7 \text{ s}^{-1}$, respectively. We may then re-estimate the non-radiative decay rate constants by taking into consideration both the ${}^3\text{LLCT}$ and ${}^3\text{IL}$ excited states with Boltzmann populations. As ${}^3\text{LLCT}$ is calculated to be $\sim 500 \text{ cm}^{-1}$ below ${}^3\text{IL}$ for complex **1**, the re-estimated non-radiative decay rate constant for complex **1** at room temperature is comparable to the experimental value ($k_{\text{nr}}(\text{calc}) \sim 1.6 \times 10^7 \text{ s}^{-1}$ and $k_{\text{nr}}(\text{expt}) \sim 5.9 \times 10^7 \text{ s}^{-1}$). In other words, the major deactivating channel for the emissive excited state of **1** is not ${}^3\text{dd}$ or ${}^3\text{LMCT}$, as is usually ascribed to efficient non-radiative decay for luminescent transition metal complexes, but ${}^3\text{LLCT}$ due to a large SOC, a large solvent reorganization energy, and the non-planar torsional motion between the $[\text{C}^{\text{N}}\text{C}]$ and arylacetylide ligands. For **3-endo**, the ${}^3\text{LLCT}$ excited state is calculated to be $\sim 1400 \text{ cm}^{-1}$ above that of the ${}^3\text{IL}$ state. Therefore, the re-estimated k_{nr} becomes $\sim 1.5 \times 10^4 \text{ s}^{-1}$, which is in good agreement with the values derived from the experimental measurements in solutions at 298 K ($k_{\text{nr}}(\text{expt}) \sim 6.8 \times 10^4 \text{ s}^{-1}$).

Based on the above analyses on non-radiative decay rate constants, it is the presence of the close-lying ${}^3\text{LLCT}$ excited state that contributes to the very fast non-radiative decay rate. The relative order of the ${}^3\text{LLCT}$ and ${}^3\text{IL}$ excited states would thus be important in determining the phosphorescence efficiency. In the present series of gold(III) complexes, this relative order can be understood from the relative energies of the $\pi(\text{C}^{\text{N}}\text{C})$ and $\pi(\text{C}\equiv\text{CPh-4-OMe})$ MOs. As the LLCT excited state is a charge transfer excited state, while the IL excited state is localized, the singlet–triplet splitting of LLCT excited states ($E({}^1\text{LLCT}) - E({}^3\text{LLCT})$) would be smaller than that of IL excited states ($E({}^1\text{IL}) - E({}^3\text{IL})$). In the case of **1**, due to the large orbital energy difference ($\Delta\varepsilon$) between the $\pi(\text{C}_\text{H}^{\text{N}}\text{C})$ and $\pi(\text{C}\equiv\text{CPh-4-OMe})$ MOs (Fig. 2), the ${}^1\text{IL}$ excited state is much higher in energy than that of the ${}^1\text{LLCT}$ excited state. Thus, the splitting of the ${}^3\text{IL}$ and ${}^3\text{LLCT}$ states is the smallest (see Fig. 6 for a schematic illustration). For **3-endo**, as the corresponding $\Delta\varepsilon$ is smaller than that of **1**, the ${}^1\text{LLCT}$ is only slightly lower in energy than the ${}^1\text{IL}$ excited state such that the ${}^3\text{IL}$ – ${}^3\text{LLCT}$ energy gap widens. For **3-exo**, as the lowest singlet excited state is predominantly IL in character, the ${}^3\text{IL}$ – ${}^3\text{LLCT}$ energy gap is even wider. In fact, we have not been able to locate a T_1 minimum corresponding to a ${}^3\text{LLCT}$ excited state (Fig. 6).

Based on the above rationale, it is speculated that the ${}^3\text{IL}$ – ${}^3\text{LLCT}$ gap of **2** should fall between that of **1** and **3-endo**, as



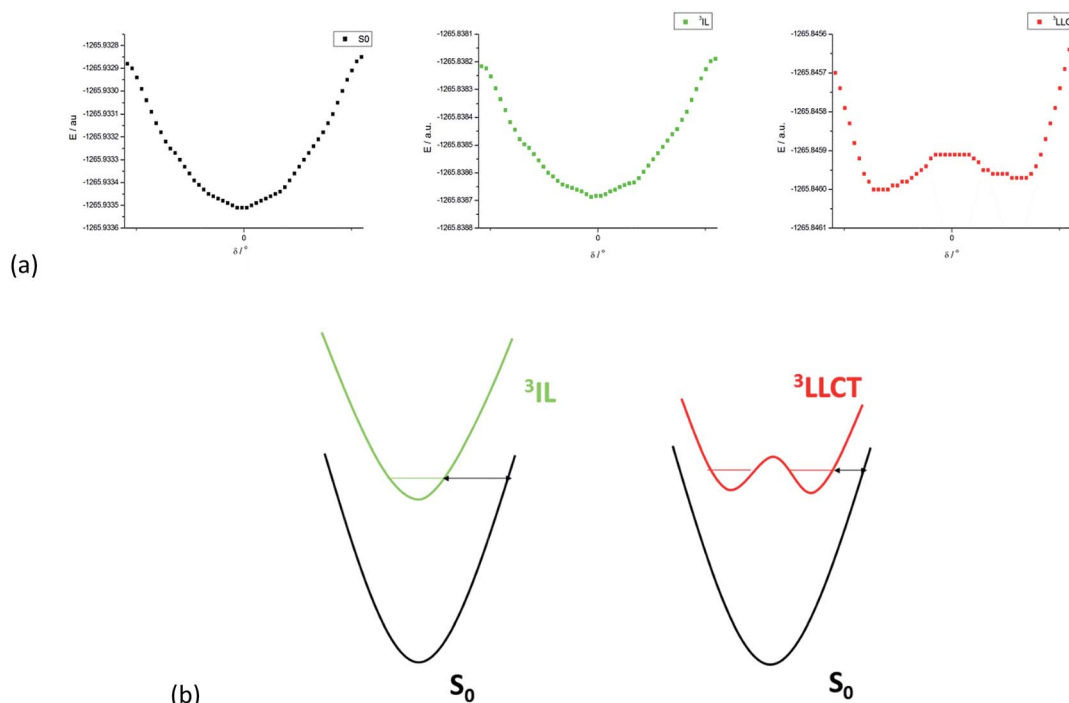


Fig. 5 (a) Potential energy surface (PES) of **1** along the torsion coordinate (δ) for the S_0 state (left), 3IL excited state (middle), and 3LLCT excited state (right). (b) The left-hand PESs depict the case when both PESs in a transition are harmonic and the right-hand PESs represent the case when the emitting excited state has a double minimum PES; the double arrow indicates the "barrier width" and it is smaller for the right-hand case than the left-hand case.

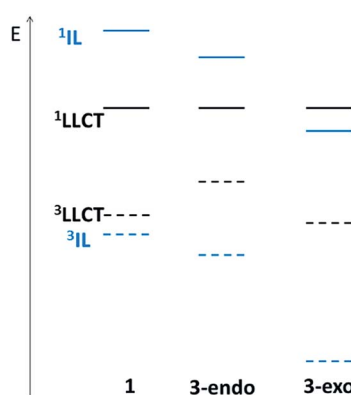


Fig. 6 Schematic representation of the relative 3LLCT – 1LLCT and 3IL – 1IL splittings for **1** (left), **3-endo** (middle), and **3-exo** (right). The solid curve corresponds to a singlet excited state while the dashed line a triplet excited state. The colours black and blue represent the LLCT and IL excited states, respectively.

deduced from the relative order of the $\pi(C_{np}^{\pi}N^{\pi}C)$ and $\pi(C\equiv CPh-4-OMe)$ MOs depicted in Fig. 2. Indeed, an energy minimum of a 3LLCT excited state was located in the course of LR-TDDFT optimization; subsequent SS-TDDFT calculation at this geometry showed that this 3LLCT excited state is *lower-lying* than the 3IL one. However, global hybrid density functionals, (e.g., PBE0, a functional that we have employed in the present work) generally underestimate the energy of charge transfer excited states within the TDDFT framework. Thus, we

performed UDFT optimization starting from these TDDFT-optimized structures (which have a stable wavefunction) to see if there is a 3LLCT excited state minimum. Unfortunately, UDFT optimization starting from the TDDFT-optimized 3LLCT excited state went back to the 3IL excited state. It is likely that this 3LLCT excited state is metastable and exhibits vibronic coupling with other close-lying excited states.

Conclusions

We have carried out a detailed theoretical study on four gold(III) $[C^{\pi}N^{\pi}C]$ cyclometalated complexes with different extents of π -conjugation. It is commonly prescribed that a rigid ligand in a transition metal complex can minimize structural distortion between the emitting triplet excited state and the ground state, thereby decreasing the non-radiative decay rate. Franck–Condon analyses on the $^3\pi^*(C^{\pi}N^{\pi}C)$ IL $\rightarrow S_0$ transitions of the four gold(III) complexes confirmed that an increase in π -conjugation at the $[C^{\pi}N^{\pi}C]$ cyclometalated ligand results in a more rigid transition metal complex, as reflected by the effective Huang–Rhys factor, S_M : **1** $>$ **2** $>$ **3-exo** and **3-endo**. Although this trend correlates with the experimentally determined non-radiative rate constants, $1 \gg 2 > 3$ -exo, the calculated k_{nr} of the $^3IL \rightarrow S_0$ transition is inconsistent with the experimental data if one also takes into consideration the 3IL – S_0 energy gap. DFT/TDDFT calculations reveal that there is an additional triplet excited state minimum, $^3[\pi(C\equiv CPh-4-OMe) \rightarrow \pi^*(C^{\pi}N^{\pi}C)]$ LLCT, for complexes **1** and **3-endo**, but not for **3-exo**. It was



found that the non-radiative decay rate constant for this ${}^3\text{LLCT} \rightarrow \text{S}_0$ transition exceeds 10^7 s^{-1} , which is more than three orders of magnitude faster than the k_{nr} for the ${}^3\text{IL} \rightarrow \text{S}_0$ transition. More importantly, if the relative splitting between the ${}^3\text{LLCT}$ and ${}^3\text{IL}$ excited states was included in estimating the k_{nr} of complexes **1** and **3-endo**, the calculated and experimental k_{nr} are in *quantitative* agreement. Based on the analysis of the relative order of $\pi(\text{C}^{\text{N}}\text{C})$ and $\pi(\text{C}\equiv\text{CPh-4-OMe})$ MOs, one could rationalize why complexes **1** and **3-endo**, but not **3-exo**, have low-lying ${}^3\text{LLCT}$ excited states. Our present analysis highlights the importance of the relative order of the frontier MOs of the coordinating ligands in multi-chromophoric transition metal complexes in designing strongly luminescent transition metal complexes. It also challenges the presumption that the low phosphorescence efficiency of transition metal complexes is due to the close proximity of the dd ligand-field state to the emitting triplet excited state.

Appendix

List of definitions, abbreviations, and symbols

Abbreviation Definition

IL	Intraligand
LLCT	Ligand-to-ligand charge transfer
LMCT	Ligand-to-metal charge transfer
MLCT	Metal-to-ligand charge transfer
SOC	Spin-orbit coupling
LR	Linear response
SS	State-specific
EQ	Equilibrium
NEQ	Non-equilibrium
PCM	Polarizable continuum model
FCF	Franck-Condon factor
PES	Potential energy surface
Expt	Experimental
Calc	Calculated
eddm	Electron difference density map
μ^{GS}	Dipole moment of the ground state
μ^{T_1}	Dipole moment of the T_1 excited state
c_{d}	Coefficient of $\text{Au}(\text{d-orbital})$
Q_0^{GS}	Optimized ground state (GS) geometry
Q_0^{ES}	Optimized excited state (ES) geometry
$\Delta E_{\text{em}}^{\text{SS}}$	Emission energy evaluated within the state-specific (SS) approach; eqn (1), Fig. 1
$E_{\text{EQ}}^{\text{ES}}(Q_0^{\text{ES}})$	Energy of the <i>excited</i> state (ES) with <i>equilibrium</i> (EQ) solvation at the optimized excited state geometry, Fig. 1
$E_{\text{NEQ}}^{\text{GS}}(Q_0^{\text{ES}})$	Energy of the <i>ground</i> state (GS) with <i>non-equilibrium</i> (NEQ) solvation at the optimized excited state geometry, Fig. 1
$E_{\text{EQ}}^{\text{GS}}(Q_0^{\text{ES}})$	Energy of the <i>ground</i> state (GS) with <i>equilibrium</i> (EQ) solvation at the optimized excited state geometry, Fig. 1
$E_{\text{EQ}}^{\text{GS}}(Q_0^{\text{GS}})$	Energy of the <i>ground</i> state (GS) with <i>equilibrium</i> (EQ) solvation at the optimized ground state geometry, Fig. 1
λ_s^{SS}	Solvent reorganization energy; eqn (2)
λ_V^{SS}	Intramolecular reorganization energy evaluated within the state-specific (SS) approach; eqn (3)
λ_V^{FC}	Intramolecular reorganization energy obtained from Franck-Condon (FC) calculation; eqn (13)

(Contd.)

Abbreviation Definition

v'	Vibrational quantum number of the first triplet (T_1) excited state
v''	Vibrational quantum number of the ground state (S_0)
$\chi_{v'}$	Vibrational wavefunction of the T_1 excited state
$\chi_{v''}$	Vibrational wavefunction of the ground state
η	Solvent refractive index
$\mathbf{M}_{\text{T}}^{\alpha}(Q)$	Transition dipole moment of the $\text{T}_1^{\alpha} \rightarrow \text{S}_0$ transition at geometry, Q
$\mathbf{M}_{\text{T}}^{\alpha}(Q_0^{\text{T}_1})$	Transition dipole moment of the $\text{T}_1^{\alpha} \rightarrow \text{S}_0$ transition evaluated at the optimized T_1 geometry, $Q_0^{\text{T}_1}$; eqn (9)
$\mathbf{M}_{\text{S}_m, j}(Q_0^{\text{T}_1})$	j -axis projection of the transition dipole moment of the $\text{S}_m \rightarrow \text{S}_0$ transition evaluated at the optimized T_1 geometry, $Q_0^{\text{T}_1}$; $j = x, y, \text{ or } z$
$I(\tilde{\nu})$	Emission intensity at $(\tilde{\nu})$
$\langle \tilde{\nu} \rangle_{\text{fcf}}$	Franck-Condon factor weighted emission energy; eqn (7)
H_{SOC}	Spin-orbit coupling operator
ΔE_{00}	Zero-point energy difference between the emitting state and the ground state
$\hbar\omega_j$	Vibrational frequency of the j^{th} normal mode (in cm^{-1})
ΔQ_j	Equilibrium displacement of the j^{th} normal mode
S_j	Huang-Rhys factor of the j^{th} normal mode; eqn (12c)
$\hbar\omega_{\text{lf}}$	Vibrational frequency of the low-frequency (lf) normal modes: $\hbar\omega_{\text{lf}} \leq 1000 \text{ cm}^{-1}$
λ_{lf}	Intramolecular reorganization energy contributed by the low-frequency (lf) normal modes; eqn (12b)
$\hbar\omega_m$	Vibrational frequency of the high-frequency (hf) normal modes in the range: $1000 < \hbar\omega_m \leq 1800 \text{ cm}^{-1}$
$\hbar\omega_M$	Mean frequency of the high-frequency normal modes, ω_m ; eqn (14c)
λ_M	Intramolecular reorganization energy contributed by the high-frequency normal modes ω_m ; eqn (14b)
S_M	Effective electron-phonon coupling strength or Huang-Rhys factor of the effective normal mode, ω_M ; eqn (12d) and (14a)
n_M	Number of vibrational quanta of $\hbar\omega_M$; eqn (12e)

Acknowledgements

This work was supported by the National Key Basic Research Program of China (no. 2013CB834802), the University Grants Committee of HKSAR (the Area of Excellence Scheme: AoE/P-03/08), the Research Grants Council of HKSAR (HKU 700812P), and the Hong Kong UGC Special Equipment Grant (SEQ HKU09). GSMT would like to give special thanks to Dr Fernando Clemente for his useful advice in using G09.

Notes and references

- (a) B. Bertrand and A. Casini, *Dalton Trans.*, 2014, 4209–4219; (b) A. Bindoli, M. P. Rigobello, G. Scutari, C. Gabbiani, A. Casini and L. Messori, *Coord. Chem. Rev.*, 2009, 293, 1692–1707; (c) C.-M. Che and R. W.-Y. Sun, *Chem. Commun.*, 2011, 47, 9554–9560; (d) S. Nobili, E. Mini, I. Landini, C. Gabbiani, A. Casini and L. Messori, *Med. Res. Rev.*, 2010, 30, 550–580; (e) R. W.-Y. Sun and C.-M. Che, *Coord. Chem. Rev.*, 2009, 293, 1682–1691.
- (a) B. Alcaide and P. Almendros, *Acc. Chem. Res.*, 2014, 47, 939–952; (b) L. Fensterbank and M. Malacria, *Acc. Chem.*



Res., 2014, **47**, 953–965; (c) D. J. Gorin, B. D. Sherry and F. D. Toste, *Chem. Rev.*, 2008, **108**, 3351–3378; (d) *Modern Gold Catalyzed Synthesis*, ed. A. S. K. Hashmi and F. D. Toste, Wiley VCH, Weinheim, Germany, 2012.

3 (a) W.-P. To, K. T. Chan, G. S. M. Tong, C. Ma, W.-M. Kwok, X. Guan, K.-H. Low and C.-M. Che, *Angew. Chem., Int. Ed.*, 2013, **52**, 6648–6652; (b) T. N. Zehnder, O. Blaque and K. Venkatesan, *Dalton Trans.*, 2014, 11959–11972.

4 C. Bronner and O. S. Wenger, *Dalton Trans.*, 2011, 12409–12420.

5 (a) V. K.-M. Au, K. M.-C. Wong, N. Zhu and V. W.-W. Yam, *J. Am. Chem. Soc.*, 2009, **131**, 9076–9085; (b) K. M.-C. Wong, L.-L. Hung, W. H. Lam, N. Zhu and V. W.-W. Yam, *J. Am. Chem. Soc.*, 2007, **129**, 4350–4365.

6 (a) A. M. Prokhorov, T. Hofbeck, R. Czerwieniec, A. F. Suleymanova, D. N. Kozhevnikov and H. Yersin, *J. Am. Chem. Soc.*, 2014, **136**, 9637–9642; (b) G. S. M. Tong and C.-M. Che, *Chem.-Eur. J.*, 2009, **15**, 7225–7237; (c) J. A. Treadway, B. Loeb, R. Lopez, P. A. Anderson, F. R. Keene and T. J. Meyer, *Inorg. Chem.*, 1996, **35**, 2242–2246.

7 N. H. Damrauer, T. R. Boussie, M. Devenney and J. K. McCusker, *J. Am. Chem. Soc.*, 1997, **119**, 8253–8268.

8 (a) V. K.-M. Au, D. P.-K. Tsang, K. M.-C. Wong, M.-Y. Chan, N. Zhu and V. W.-W. Yam, *Inorg. Chem.*, 2013, **52**, 12713–12725; (b) W.-P. To, G. S. M. Tong, W. Lu, C. Ma, J. Liu, A. L.-F. Chow and C.-M. Che, *Angew. Chem., Int. Ed.*, 2012, **51**, 2654–2657.

9 S. C. F. Kui, F.-F. Hung, S.-L. Lai, M.-Y. Yuen, C.-C. Kwok, K.-H. Low, S. S.-Y. Chui and C.-M. Che, *Chem.-Eur. J.*, 2012, **18**, 96–109.

10 (a) A. Pedone, *J. Chem. Theory Comput.*, 2013, **9**, 4087–4096; (b) R. Improta, G. Scalmani, M. J. Frisch and V. Barone, *J. Chem. Phys.*, 2007, **127**, 074501–074509.

11 F. J. A. Ferrer, J. Cerezo, J. Soto, R. Improta and F. Santoro, *Comput. Theor. Chem.*, 2014, **1040**–**1041**, 328–337.

12 G. S. M. Tong, P. K. Chow, W.-P. To, W.-M. Kwok and C.-M. Che, *Chem.-Eur. J.*, 2014, **20**, 6433–6443.

13 S. J. Strickler and R. A. Berg, *J. Chem. Phys.*, 1962, **37**, 814–822.

14 B. S. Brunschwig and N. Sutin, *Comments Inorg. Chem.*, 1987, **6**, 209–235.

15 C. Adamo and V. Barone, *J. Chem. Phys.*, 1999, **110**, 6158–6169.

16 M. J. Frisch, G. W. Trucks, H. B. Schlegel, G. E. Scuseria, M. A. Robb, J. R. Cheeseman, G. Scalmani, V. Barone, B. Mennucci, G. A. Petersson, H. Nakatsuji, M. Caricato, X. Li, H. P. Hratchian, A. F. Izmaylov, J. Bloino, G. Zheng, J. L. Sonnenberg, M. Hada, M. Ehara, K. Toyota, R. Fukuda, J. Hasegawa, M. Ishida, T. Nakajima, Y. Honda, O. Kitao, H. Nakai, T. Vreven, J. A. Montgomery, Jr., J. E. Peralta, F. Ogliaro, M. Bearpark, J. J. Heyd, E. Brothers, K. N. Kudin, V. N. Staroverov, R. Kobayashi, J. Normand, K. Raghavachari, A. Rendell, J. C. Burant, S. S. Iyengar, J. Tomasi, M. Cossi, N. Rega, J. M. Millam, M. Klene, J. E. Knox, J. B. Cross, V. Bakken, C. Adamo, J. Jaramillo, R. Gomperts, R. E. Stratmann, O. Yazyev, A. J. Austin, R. Cammi, C. Pomelli, J. W. Ochterski, R. L. Martin, K. Morokuma, V. G. Zakrzewski, G. A. Voth, P. Salvador, J. J. Dannenberg, S. Dapprich, A. D. Daniels, Ö. Farkas, J. B. Foresman, J. V. Ortiz, J. Cioslowski and D. J. Fox, *Gaussian 09 (Revision C.01)*, Gaussian, Inc., Wallingford CT, 2009.

17 (a) M. M. Franel, W. J. Petro, W. J. Hehre, J. S. Binkley, M. S. Gordon, D. J. DeFree and J. A. Pople, *J. Chem. Phys.*, 1982, **77**, 3654; (b) P. C. Hariharan and J. A. Pople, *Theor. Chem. Acc.*, 1973, **28**, 213.

18 (a) D. Andrae, U. Haeussermann, M. Dolg, H. Stoll and H. Preuss, *Theor. Chim. Acta*, 1990, **77**, 123–141; (b) J. M. L. Martin and A. Sundermann, *J. Chem. Phys.*, 2001, **114**, 3408–3420.

19 M. Cossi, G. Scalmani, N. Rega and V. Barone, *J. Chem. Phys.*, 2002, **117**, 43–54.

20 R. Improta, V. Barone, G. Scalmani and M. J. Frisch, *J. Chem. Phys.*, 2006, **125**, 054101–054109.

21 R. Englman and J. Jortner, *Mol. Phys.*, 1970, **18**, 145–164.

22 M. Pabst, D. Sundholm and A. Köhn, *J. Phys. Chem. C*, 2012, **116**, 15203–15217.

23 (a) J. Cerezo, J. Zúñiga, A. Requena, F. J. Á. Ferrer and F. Santoro, *J. Chem. Theory Comput.*, 2013, **9**, 4947–4958; (b) J. R. Reimers, *J. Chem. Phys.*, 2001, **115**, 9103–9109; (c) E. L. Sibert III, J. T. Hynes and W. P. Reinhardt, *J. Phys. Chem.*, 1983, **87**, 2032–2037.

24 R. Li and E. C. Lim, *J. Chem. Phys.*, 1972, **57**, 605–612.

